Frontiers of Information Technology & Electronic Engineering
www.jzus.zju.edu.cn; engineering.cae.cn; www.springerlink.com
ISSN 2095-9184 (print); ISSN 2095-9230 (online)
E-mail: jzus@zju.edu.cn

Development of a novel autonomous lower extremity exoskeleton robot for walking assistance*

Yong HE[1,2,3], Nan LI[1,2], Chao WANG[1,2], Lin-qing XIA[1,2], Xu YONG[4], Xin-yu WU†‡[1,2]

[1]*Guangdong Provincial Key Laboratory of Robotics and Intelligent System, Shenzhen Institute of Advanced Technology, Chinese Academy of Sciences, Shenzhen 518055, China*

[2]*CAS Key Laboratory of Human-Machine Intelligence-Synergy Systems, Shenzhen Institute of Advanced Technology, Chinese Academy of Sciences, Shenzhen 518055, China*

[3]*Shenzhen College of Advanced Technology, University of Chinese Academy of Sciences, Shenzhen 518055, China*

[4]*Department of Mechanical Engineering and Intelligent Systems, the University of Electro-Communications, Tokyo 182-8585, Japan*

†E-mail: xy.wu@siat.ac.cn

Received Sept. 14, 2018; Revision accepted Feb. 1, 2019; Crosschecked Mar. 14, 2019

Abstract: Today, exoskeletons are widely applied to provide walking assistance for patients with lower limb motor incapacity. Most existing exoskeletons are under-actuated, resulting in a series of problems, e.g., interference and unnatural gait during walking. In this study, we propose a novel intelligent autonomous lower extremity exoskeleton (Auto-LEE), aiming at improving the user experience of wearable walking aids and extending their application range. Unlike traditional exoskeletons, Auto-LEE has 10 degrees of freedom, and all the joints are actuated independently by direct current motors, which allows the robot to maintain balance in aiding walking without extra support. The new exoskeleton is designed and developed with a modular structure concept and multi-modal human-robot interfaces are considered in the control system. To validate the ability of self-balancing bipedal walking, three general algorithms for generating walking patterns are researched, and a preliminary experiment is implemented.

Key words: Lower-limb; Exoskeleton; Self-balancing; Bipedal walking; Modular design
https://doi.org/10.1631/FITEE.1800561 **CLC number:** TP23

1 Introduction

The problem of lower limb motor incapacity, caused by diseases like multiple sclerosis, muscle atrophy, stroke, polio, and spinal cord injury (SCI), is a limitation for many people. SCI is the primary condition causing lower limb disabilities. According to one statistic in National Spinal Cord Injury Statistical Center (2016), there are about 288 000 individuals with SCI in the United States, and the number of such cases is growing by about 17 700 new cases each year. About 58.7% of SCI patients are tetraplegic and 40.6% are paraplegic. Approximately 17 576 Americans lose total or partial lower limb mobility because of SCI annually. These patients can merely lie in a bed or simply move with a wheelchair, which may lead to multiple secondary medical conditions including muscle atrophy, osteoporosis, and stress ulcers (McDonald and Sadowsky, 2002), and causing secondary injury and pain for patients and their families. Hence, recovery of the ability to walk and stand is urgent and necessary for these patients (Brown-Triolo et al., 2002).

‡ Corresponding author

* Project supported by the Shenzhen Robotics Research Center Project, the National Natural Science Foundation of China (No. U1613219), the Shenzhen Technology Project, China (No. JSGG20160301160759264), and the Shenzhen Overseas Innovation and Entrepreneurship Research Program, China (No. KQJSCX20170731164301774)

ORCID: Xin-yu WU, http://orcid.org/0000-0001-6130-7821

With the development of robotics and control technology over the past few decades, the exoskeleton as a significant branch of robotics has been well developed. Many institutions have conducted research in the exoskeleton field. Early studies of exoskeletons were mostly military-oriented, aiming at increasing the ability of soldiers to carry loads. BLEEX (Zoss, 2006), ExoHiker, and HULC (Kopp, 2011), developed by the Berkeley Robotics & Human Engineering Laboratory, were powered by hydraulic systems and can offer assistance at the hip, ankle, and knee joints. As motor technology improves, more and more civil-oriented, lightweight, miniaturized, and electric-driven exoskeletons have emerged (Mertz, 2012). The hybrid assistive limb (HAL), developed by the Japanese company CYBERDYNE Inc., is an exoskeleton system for helping senior citizens with lower limb functional degeneration or patients with lower limb paralysis. The exoskeleton is driven by direct current (DC) motors and can assist the extension/flexion movements of the hip, knee, and ankle joints, helping wearers with daily activities like walking, standing, and climbing up and down stairs (Tsukahara et al., 2015). The HAL power modules can generate assist torque by amplifying the estimated joint torque based on the wearer's own electromyographic signals, and thus the wearer's movement control can be realized. In addition to HAL, many medical commercial exoskeletons have emerged in recent years, such as AILEGS by Beijing Ai-robotics Ltd. (https://www.ai-robotics.cn/), Ekso GT by Ekso Bionics (https://eksobionics.com/), Indego by Parker Hannifin (http://www.indego.com/), ReWalk by Argo Medical Technologies Ltd. (Talaty et al., 2013; Gardner et al., 2017), Fourier M2 by Shanghai Fourier Science and Technology Ltd. (http://www.fftai.com/product/lowerLimbs.php), and REX by Rex Bionics Ltd. in New Zealand (https://www.rexbionics.com/).

Because of its simple mechanical structure and easy control mode, the "hip+knee actuated" structure is widespread in the exoskeleton field, such as SIAT Exoskeleton, eLEGS, ABLE, EXPOS, SUBAR, and WPAL (Kong and Jeon, 2006; Fang et al., 2008; Kong et al., 2009; Strausser et al., 2010; Mori et al., 2011; Zhang et al., 2016). Although the above devices are slightly different in degrees of freedom (DOFs) and layout, these exoskeletons are actuated with only DC motors at the hip and knee joints. As a result, crutches are needed as extra support to keep the wearer's balance.

Based on our investigation, most existing lower limb exoskeletons have fewer active joints or DOFs than human legs, which means that the device will interfere with the wearer's body during walking. Due to the lack of active DOFs, the wearer's body can adapt to only lower limb exoskeletons by walking with an unnatural gait. The wearer needs to spend more time and energy practicing, which is not conducive to rehabilitation of the patient. To solve this dilemma, we need to build a more ergonomic lower limb exoskeleton to avoid mobility issues for the wearer. Thus, we propose a novel intelligent autonomous lower extremity exoskeleton (Auto-LEE). Compared with other exoskeletons, Auto-LEE can provide the wearer with a self-balancing platform without the need for additional support, such as crutches. In addition, Auto-LEE can be controlled through an integrated multi-modal human-robot interface, e.g., electroencephalogram (EEG), electromyogram (EMG), or a joystick, which greatly enriches the selectivity of the control mode.

The main purpose of the exoskeleton is to assist the wearer in walking. To achieve stable walking of the robot, its walking pattern should be planned and controlled. The former is implemented by a walking pattern generator, and the latter is accomplished by a walking stabilizer. To validate the self-balancing walking ability, we focus only on the algorithms for walking pattern generation to realize a preliminary walking experiment in this study.

2 Biomechanical analysis of the human body

To achieve the most natural human gait as close as possible and increase the application range of the exoskeleton, we analyze human biomechanical properties. The modular design concept is introduced into the structure development to improve usage and maintenance convenience.

The fundamental biomechanical considerations for the exoskeleton design are factors such as the number of DOFs, structure morphology, range-of-motion (ROM), joint category, driving pattern, load weight, and wearable mode (Cenciarini and Dollar, 2011).

Table 2 Dimension values of the exoskeleton

Variable	Value (mm)
Thigh length	425–525
Shank length	340–420
Waist width	365–440
Waist thickness	200
Ankle height	133
Foot width	130
Foot length	380

According to human anatomy (Fig. 1a), almost all human movements are contained in three principal planes: sagittal plane, coronal plane, and transverse plane. It may be broadly acknowledged that the flexion/extension motions of the joints in the sagittal plane contribute mostly to general lower limb activities, such as walking, running, squatting, standing, and climbing up/downstairs. As a result, most existing exoskeletons place motors at the hip, knee, and ankle joints. In fact, the abduction/adduction motions of the joints in the coronal plane are very important in bipedal walking, without which the wearer cannot maintain self-balance in a natural walk. To achieve self-balanced walking ability, Auto-LEE has 10 joints, and all joints are driven by DC motors. It can provide assistance in the flexion/extension motion of the hip $\theta_{\mathrm{hip\_s}}$, knee θ_{knee}, and ankle $\theta_{\mathrm{ank\_s}}$, and the abduction/adduction motion of the hip $\theta_{\mathrm{hip\_c}}$ and ankle $\theta_{\mathrm{ank\_c}}$, indicated as Fig. 1c.

Auto-LEE is a humanlike exoskeleton robot, and it is placed parallel to the wearer's limb when it operates. To achieve kinematic compliance and

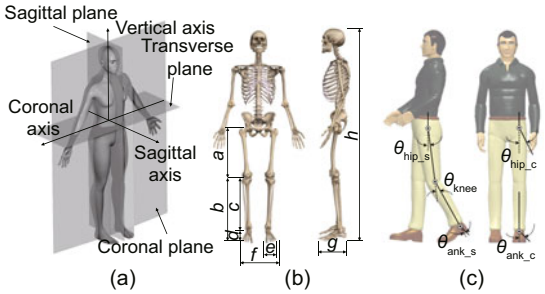

Fig. 1 Biomechanical parameters of human body: (a) main human motion planes; (b) dimension parameters; (c) related lower limb joints

Table 3 Range of motions (ROMs) of joints

Joint	Motion	Human ROM (°)	Auto-LEE ROM (°)
Hip	Extension/Flexion	[−25, +125]	[−25, +90]
	Abduction/Adduction	[−30, +60]	[−30, +30]
	Eversion/Inversion	[−30, +60]	N/A
Knee	Extension/Flexion	[0, +130]	[0, +110]
Ankle	Extension/Flexion	[−50, +30]	[−25, +30]
	Abduction/Adduction	[−35, +15]	[−30, +15]

N/A: not available

avoid interfering with natural movements, each joint center should be aligned with that of the lower limb, which means that the joint distribution, ROM, and dimension parameters of the exoskeleton should be determined by biomechanical properties. The vital human dimension parameters are shown in Fig. 1b, and the reference values of Chinese adults are listed in Table 1 (Protection and Labour, 1988). Then the values of the Auto-LEE dimension parameters, listed in Table 2, are determined according to these data. To adapt to different body sizes, the waist, shank, and thigh dimension parameters are adjustable. Table 3 and Fig. 2 show the reference ROMs of the human joints (Gao, 2004), and the ROMs of the exoskeleton joints are determined by these values.

3 Design of the exoskeleton

According to the design concept, the number of active DOFs should be chosen based on the need to meet the demand of self-balanced walking abil-

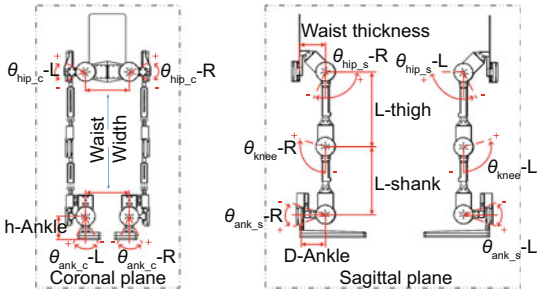

Fig. 2 Distribution and range of motion of Auto-LEE joints

Table 1 Reference dimension values of Chinese adults

Gender	Variable (mm)						
	Stature	Thigh length	Shank length	Ankle height	Foot width	Pelvis width	Foot length
Male	1604–1814	436–523	344–419	73–79	90–107	288–346	234–272
Female	1570–1697	438–494	344–390	66–69	88–98	317–360	229–251

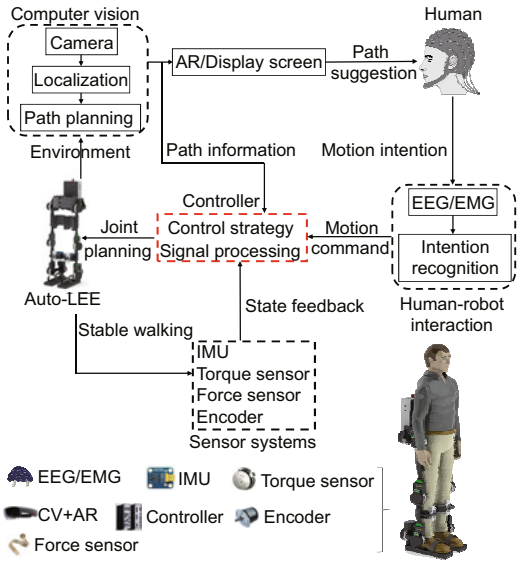

Fig. 3 Overall view of the exoskeleton system

ity, natural gait, and control complexity. To accommodate individuals with different pelvis widths and shank/thigh lengths, manual length regulators have been designed in different parts.

3.1 Overall view of the exoskeleton system

Fig. 3 shows the comprehensive design concept of Auto-LEE. The integrated system consists of five main components: an exoskeleton robot with 10 active joints, a control box, a computer vision unit (CVU), multi-modal human-robot interfaces, and sensor systems.

The CVU, which includes a camera and a microcontroller, is used to detect the surrounding environment and offers path planning information to the human and control box. After the human acquires the information by the screen or augmented reality glasses, his/her motion intention will be recognized and transferred by the human-robot interfaces. On the other hand, the control box can obtain path planning from the CVU, motion intention from the human, and the robot motion state from the sensor systems. Then it can generate commands to control the exoskeleton and realize self-balanced walking.

3.2 Design of the exoskeleton with modular structure

Fig. 4 shows the structural design of Auto-LEE in detail, where exploded views of the overall mechanical structure and a modular drive unit are presented. Ten modular drive units (M1–M10) are used within the Auto-LEE joints. Those drive units have identical interfaces and analogous structures, which create convenient assembly and maintenance. The material of most Auto-LEE structural parts is Aluminum 7075, which features light weight and high strength.

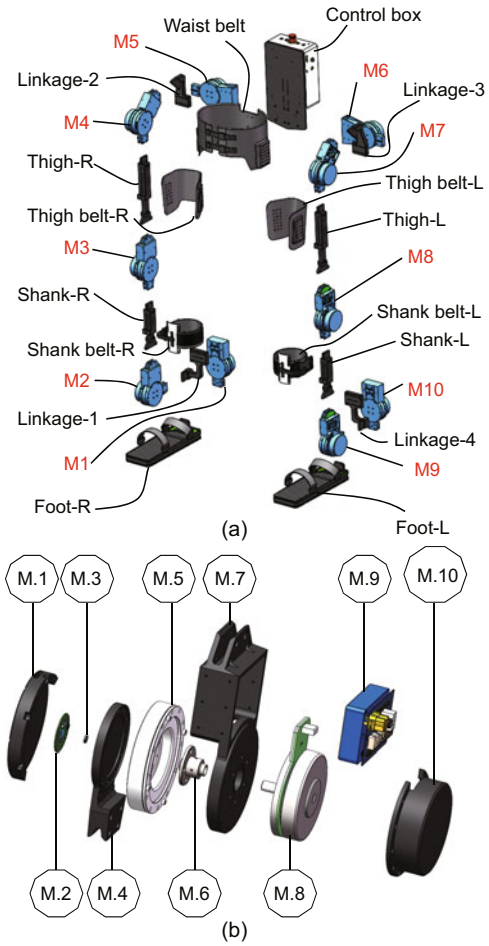

Fig. 4 Exploded views of the exoskeleton (a) and the modular drive unit (b)

As shown in Fig. 4b, the modular drive unit is made up of 10 main parts. The rotary plate (M.4) and fixed plate (M.7) are the interfaces for linking to other parts of Auto-LEE. They rotate about the axis of the electric motor (M.8), which transforms electric power to joint motion. The electric motor is a Maxon-EC-90-flat permanent magnet brushless motor, with nominal torque of 0.56 N·m (Newton meter), nominal speed of 2510 r/min (revolutions per minute), and a built-in incremental encoder. A harmonic reducer (M.5) with a reduction ratio of 160 is connected to the output shaft of the electric motor. A coupling (M.6) links M.5 and M.8, and measures

the torque transmitted with a built-in torque sensor. The servo amplifier (M.9) is accommodated in the rectangular housing. Besides driving the motor, it is used for collecting sensor signals in the drive unit and forming the Ethernet control automation technology (EtherCAT) network with other units. The end cover (M.10) is designed to protect M.8. The inhibiting device (M.1) limits the ROM of the drive unit to avoid physical injury to the user. The combination of the magnetic encoder (M.2) and the permanent magnet wafer (M.3) forms an absolute position encoder for recording the absolute joint angle.

As illustrated in Fig. 4a, the modular drive unit M5/M6, connected to the control box, controls the extension/flexion rotation of the right/left hip joint in the sagittal plane. M4/M7 is attached to M5/M6 by a J-type linkage, used for controlling the abduction/adduction revolution of the right/left hip joint in the coronal plane. Thigh-R/Thigh-L links M4/M7 and M3/M8, while Shank-R/Shank-L links M3/M8 and M2/M9. The right/left motion of the knee joint in the sagittal plane is regulated by M3/M8. M2/M9 controls the extension/flexion rotation of the right/left ankle joint in the sagittal plane, while M1/M10, linked to M2/M9 by an L-type linkage, domains the abduction/adduction rotation of the right/left ankle joint in the coronal plane. Foot-R/Foot-L is attached to M1/M10. Therefore, Auto-LEE has 10 active DOFs in the joint space to generate flexible gaits. To accommodate various users, Auto-LEE has manual length regulators on the thigh, shank, waist, and ankle (Fig. 3). By changing the position of the fastening screws, the lengths of thighs and shanks, as well as the width of the waist, can be adjusted.

Due to the flexibility of human tissue, it is not easy to firmly fasten the exoskeleton to the user in a comfortable way. The binding devices designed for Auto-LEE comprise rigid and soft parts on the waist, thighs, shanks, and feet for fastening to the body. The inflexible parts of the binding devices are designed to be located on the exoskeleton, while soft belts bind the devices to the human body.

3.3 Design of the plantar pressure detection system

Auto-LEE is designed to be self-balancing during walking without the support of extra devices like crutches, which are used in most lower limb exoskeletons. Most existing strategies for stable walking control of legged robots are based on the zero moment point (ZMP) theory. Hence, tracking the ZMP position and maintaining it within the foot support area during walking are extremely important. Several approaches can be used to obtain the position of the ZMP; one of them is to calculate the ZMP position based on the model of the exoskeleton together with the data from the provided encoders. A more direct way is to measure the force/torque applied on the planar using sensors underneath the foot. In this study, a plantar pressure detection system (PPDS) based on one-dimensional force sensors, is devised to measure the ZMP position in real time. After obtaining the data from the force sensors, the coordinate value (P_x, P_y) of the ZMP location can be calculated (Vukobratović and Borovac, 2004):

$$P_x = \frac{\sum_{j=1}^{N} r_{jx} f_j}{\sum_{j=1}^{N} f_j}, \quad P_y = \frac{\sum_{j=1}^{N} r_{jy} f_j}{\sum_{j=1}^{N} f_j}, \tag{1}$$

where f_j denotes the force measured by the j^{th} sensor, whose coordinate value is (r_{jx}, r_{jy}), and N represents the number of force sensors in one foot.

Fig. 5 illustrates the structural design of the PPDS. Two aluminum boards, the upper baseboard (F.3) and the lower baseboard (F.9), make up the main framework of the PPDS. These two parts are linked through eight guide posts (F.7), so they can slide relative to each other. When there is no pressure applied on F.3, the springs (F.6) separate the aluminum boards. At the bottom of F.3, 12 thin flexible piezoresistive force sensors (F.4) are attached for measuring one-dimensional force. To increase the measurement accuracy, each sensor's sensing area is covered by a rubber pad (F.5). A spongy cushion

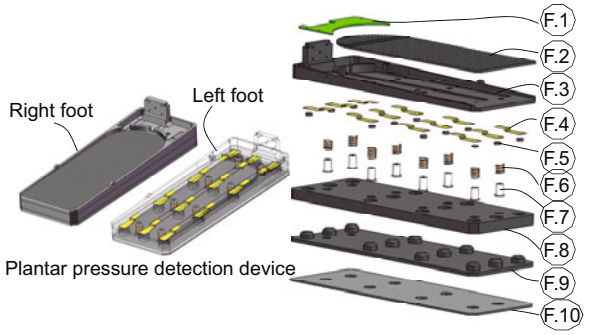

Fig. 5 Plantar pressure detection device of the exoskeleton

(F.8) is inserted between F.3 and F.9 to absorb shock each time the foot contacts the floor. To increase the contact friction, an antiskid mat (F.2) and a rubber sole (F.10) are attached on the top of F.3 and at the bottom of F.9, respectively. The control board (F.1), which is set in F.3, is employed to process the data output from the sensors and convey the data into the Auto-LEE controller through a controller area network (CAN).

3.4 Design of the control system

Fig. 6 shows the layout of the Auto-LEE control architecture, which is defined to integrate the subsystems and is described below.

3.4.1 Control unit

This unit is the core of the entire control system and consists of a main controller (a high-performance PC with a real-time operating system) and several interface modules including universal serial bus (USB)-CAN adapters, EtherCAT adapters, and serial interfaces. Its responsibility is to collect information from different subsystems, process the signals, and execute the control algorithms to generate motion signals for the motor drivers.

3.4.2 Motor driver unit

There are 10 motor driver units, attached in the joints of the exoskeleton, and each of them is formed by a servo amplifier and a printed circuit board (PCB). The driver unit powers and drives the actuator, collects measurement data from the encoder and torque sensor, and exchanges information with the controller and other driver units through an EtherCAT network.

3.4.3 Sensor system

Various sensors, such as inertial measurement units (IMUs) and force sensors, are placed in different parts to check the motion state of the exoskeleton. Twelve force sensors and a six-axis IMU are embedded in the left/right foot, and the signals from these sensors are acquired and processed by a PCB with an STM32F103 microprocessor. Seven other six-axis IMUs are installed in the thigh, shank, and waist to detect movement. All the measurement data are delivered to the controller through the CAN I network.

3.4.4 Multi-modal human-robot interfaces

The human-robot interfaces, which include EEG, EMG, joystick, and camera, are used for signal interaction between the device and users, and all their data are transmitted to the control unit through the CAN II network.

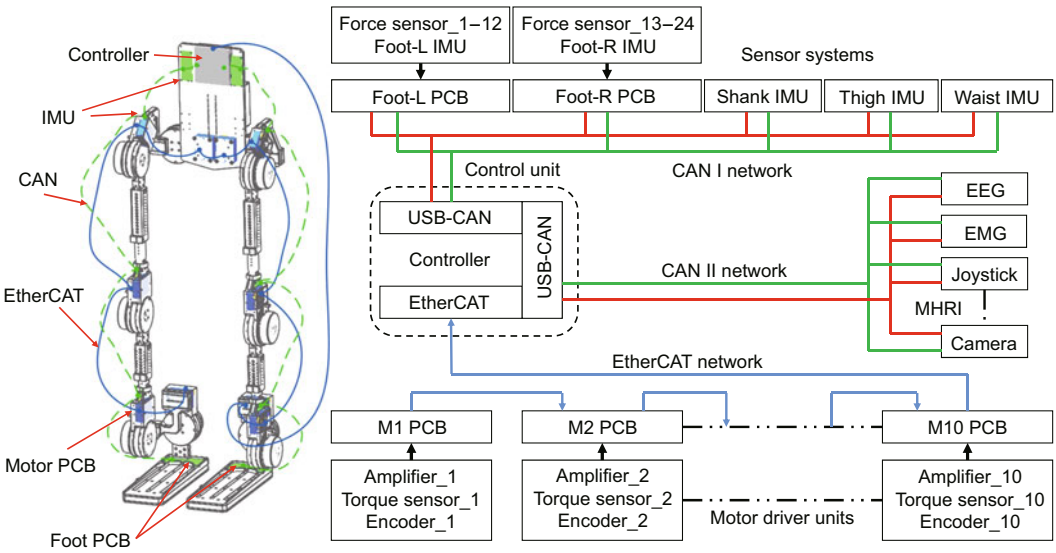

Fig. 6 Overall view of the control architecture

4 Preliminary research on self-balanced walking of the exoskeleton

In terms of control, Auto-LEE can be treated as a bipedal robot with a large disturbance, which is the human wearing the exoskeleton. In this study, we focus only on validating the ability of self-balanced walking of the exoskeleton itself, ignoring the human disturbance. Theories on bipedal humanoid robots have been researched for decades, and we will discuss three general algorithms for walking pattern generation in this section. Before that, the details of building the kinematic model are introduced.

4.1 Kinematic analysis of the exoskeleton

The kinematic model of the Auto-LEE robot can be simplified as a seven-link model (Fig. 7). The world coordination (O_{w}-xyz) is defined as follows: the x axis pointing directly in front of the robot, the z axis pointing directly above the robot, and the y axis is determined by the right-hand rule. Then we can build coordination in each joint center: right hip coordination (O_{hR}-xyz), right knee coordination (O_{kR}-xyz), right foot coordination (O_{R}-xyz), left hip coordination (O_{hL}-xyz), left knee coordination (O_{kL}-xyz), left foot coordination (O_{L}-xyz), and waist base coordination (O-xyz). The attitude matrix of each joint is equal to that of world coordination in the initial state. Axis vector $\boldsymbol{a}_j$ $(j = 1, 2, \ldots, 10)$ is along the rotation center of each joint, and θ_j is the joint angle.

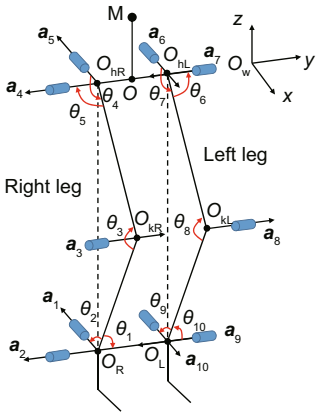

Fig. 7 Kinematic diagram of mechanism of the exoskeleton

Despite the 10 joints of the exoskeleton, we can treat it as two independent arms (the left and right legs with five joints), linked to a common base (the waist). Then the kinematics can be solved as a non-redundant problem. Thus, the forward kinematic model of each chain can be obtained with the Rodrigues rotation formula and chain rules, presented as follows:

$$\begin{cases} {}^{\mathrm{base}}\boldsymbol{T}_{\mathrm{L}} = \begin{bmatrix} \boldsymbol{R}_{\mathrm{L}} & \boldsymbol{P}_{O_{\mathrm{L}}} \\ \boldsymbol{0} & \boldsymbol{1} \end{bmatrix} = {}^{0}\boldsymbol{T}_{6}{}^{6}\boldsymbol{T}_{7}{}^{7}\boldsymbol{T}_{8}{}^{8}\boldsymbol{T}_{9}{}^{9}\boldsymbol{T}_{10}, \\ {}^{\mathrm{base}}\boldsymbol{T}_{\mathrm{R}} = \begin{bmatrix} \boldsymbol{R}_{\mathrm{R}} & \boldsymbol{P}_{O_{\mathrm{R}}} \\ \boldsymbol{0} & \boldsymbol{1} \end{bmatrix} = {}^{0}\boldsymbol{T}_{5}{}^{5}\boldsymbol{T}_{4}{}^{4}\boldsymbol{T}_{3}{}^{3}\boldsymbol{T}_{2}{}^{2}\boldsymbol{T}_{1}, \\ {}^{i}\boldsymbol{T}_{j} = \begin{bmatrix} {}^{i}\boldsymbol{R}_{j} & \boldsymbol{b}_{j} \\ \boldsymbol{0} & \boldsymbol{1} \end{bmatrix} = \begin{bmatrix} \exp(\hat{\boldsymbol{a}}_j\theta_j) & {}^{i}\boldsymbol{P}_{O_j} \\ \boldsymbol{0} & \boldsymbol{1} \end{bmatrix}, \end{cases} \tag{2}$$

where ${}^{\mathrm{base}}\boldsymbol{T}_{\mathrm{L}}/{}^{\mathrm{base}}\boldsymbol{T}_{\mathrm{R}}$ is the transformation matrix from left/right foot coordination to base coordination, $\boldsymbol{R}_{\mathrm{L}}/\boldsymbol{R}_{\mathrm{R}}$ is the attitude matrix of the left/right foot described in base coordination, and $\boldsymbol{P}_{O_{\mathrm{L}}}/\boldsymbol{P}_{O_{\mathrm{R}}}$ represents the position vector. ${}^{i}\boldsymbol{T}_{j}$ is the transformation matrix from the i^{th} joint coordination to the j^{th} joint coordination, ${}^{i}\boldsymbol{R}_{j}$ is the attitude matrix of the i^{th} joint coordination described in the j^{th} joint coordination, and $\boldsymbol{b}_j/{}^{i}\boldsymbol{P}_{O_j}$ represents the position vector.

Conversely, we can obtain the inverse kinematic models, as defined in Eq. (3), of the two arms with the geometrical analysis method:

$$\begin{cases} (\theta_6, \theta_7, \ldots, \theta_{10}) = f_{\mathrm{L}}(\boldsymbol{R}_{\mathrm{L}}, \boldsymbol{P}_{O_{\mathrm{L}}}, \boldsymbol{R}_{O}, \boldsymbol{P}_{O}), \\ (\theta_1, \theta_2, \ldots, \theta_5) = f_{\mathrm{R}}(\boldsymbol{R}_{\mathrm{R}}, \boldsymbol{P}_{O_{\mathrm{R}}}, \boldsymbol{R}_{O}, \boldsymbol{P}_{O}), \end{cases} \tag{3}$$

where $\boldsymbol{R}_{\mathrm{L}}/\boldsymbol{R}_{\mathrm{R}}/\boldsymbol{R}_{O}$ is the attitude matrix of the left foot/right foot/waist described in world coordination (O_{w}-xyz), and $\boldsymbol{P}_{O_{\mathrm{L}}}/\boldsymbol{P}_{O_{\mathrm{R}}}/\boldsymbol{P}_{O}$ represents the corresponding location vector.

4.2 Introduction of bipedal walking pattern generation algorithms

The walking pattern generation algorithms we will discuss just need a simplified model of the robot without precise knowledge of dynamics; they are the three-dimensional inverted linear pendulum mode method (3D-ILPM) (Kajita et al., 2001), the cart-table model (Kajita et al., 2003) method, and the ZMP preview control method (Katayama et al., 1985; Shimmyo et al., 2013).

4.2.1 Bipedal walking pattern generation based on 3D-ILPM

As Fig. 8a shows, in a single-foot support pattern, the dynamic model of the exoskeleton can be simplified as a three-dimensional linear inverted pendulum. The motion of the center of mass (COM) can be constrained in a plane:

$$z = k_x x + k_y y + z_c, \tag{4}$$

where k_x and k_y are the slope factors, and z_c is the z-intercept. In this study, we assume that $k_x = k_y = 0$, so the trajectory of the COM projected on the X-Y plane can be described as

$$\ddot{x} = \frac{g}{z_c} x, \quad \ddot{y} = \frac{g}{z_c} y. \tag{5}$$

After we set the n^{th} step length and step width (S_x^n, S_y^n) of the foot location planning (equal to ZMP location here), the desired location of the foot $(P_{x\text{d}}^n, P_{y\text{d}}^n)$ is determined by Eq. (6), and the motion state of the walk primitive can be calculated by Eq. (7), assuming that the left foot is the initial supporting foot:

$$\begin{bmatrix} P_{x\text{d}}^n \\ P_{y\text{d}}^n \end{bmatrix} = \begin{bmatrix} P_x^{n-1} + S_x^n \\ P_y^{n-1} + (-1)^n S_y^n \end{bmatrix}, \tag{6}$$

$$\begin{cases} \bar{x}^n = S_x^{n+1}/2, \\ \bar{y}^n = (-1)^n S_y^{n+1}/2, \\ \bar{v}_x^n = \dfrac{C+1}{T_c S} \bar{x}^n, \\ \bar{v}_y^n = \dfrac{C-1}{T_c S} \bar{y}^n, \end{cases} \tag{7}$$

where $T_c = \sqrt{z_c/g}$, $C \equiv \cosh(T_s/T_c)$, $S \equiv \sinh(T_s/T_c)$, and T_s is a single support phase.

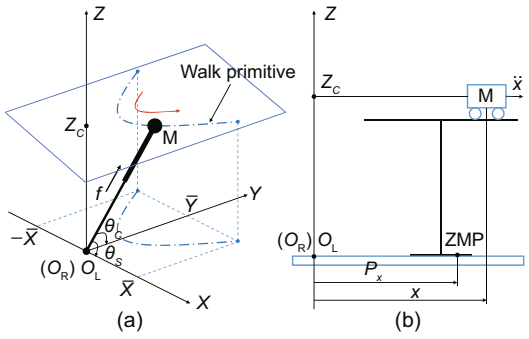

Fig. 8 Simplified dynamic model: (a) 3D-ILPM model; (b) cart-table model

When the pattern changes, the actual foot location (P_x^*, P_y^*) needs to be adjusted to meet the walking speed, and it can be calculated as follows:

$$\begin{cases} P_x^* = -\frac{a_x(C-1)}{D_x}(x^{\text{d}} - Cx_i^n - T_c S\dot{x}_i^n) \\ \qquad -\frac{b_x S}{T_c D_x}\left(\dot{x}^{\text{d}} - \frac{S}{T_c}x_i^n - C\dot{x}_i^n\right), \\ P_y^* = -\frac{a_y(C-1)}{D_y}(y^{\text{d}} - Cy_i^n - T_c S\dot{y}_i^n) \\ \qquad -\frac{b_y S}{T_c D_y}\left(\dot{y}^{\text{d}} - \frac{S}{T_c}y_i^n - C\dot{y}_i^n\right), \end{cases} \tag{8}$$

where $D_x \equiv a_x(C-1)^2 + b_x(S/T_c)^2$, $D_y \equiv a_y(C-1)^2 + b_y(S/T_c)^2$, and $(a_x, b_x, a_y, b_y > 0)$ are weighting factors.

With the algorithm above, we obtain the COM trajectory after the foot location is planned. However, when the walking pattern changes, the foot locations will be adjusted, which leads to differences between the actual walking positions and the desired ones. A numerical example will be given in Section 5.

4.2.2 Bipedal walking pattern generation based on the cart-table model

As Fig. 8b shows, in a single-foot support pattern, the dynamic model of the exoskeleton can be simplified as a cart-table model. The cart position (x, y) represents the COM location, and the ZMP position (P_x, P_y) equals the foot location. The ZMP location can be calculated as follows:

$$P_x = x - \frac{z_c}{g}\ddot{x}, \quad P_y = y - \frac{z_c}{g}\ddot{y}, \tag{9}$$

where z_c is the height of the COM. We can find that the ZMP location is the output of the system here, while it acts as the input in the algorithm based on 3D-ILPM. Thus, we can control ZMP locations with the cart-table model.

Eq. (9) can be rewritten in the discretized form:

$$\begin{cases} P_{xk} = u_k x_{k-1} + v_k x_k + w_k x_{k+1}, \\ P_{yk} = u_k y_{k-1} + v_k y_k + w_k y_{k+1}, \end{cases} \tag{10}$$

where $u_k \equiv -z_c/(g\Delta t^2)$, $v_k \equiv 2z_c/(g\Delta t^2) + 1$, and $w_k \equiv -z_c/(g\Delta t^2)$.

Then we can obtain the discretized ZMP locations of all intervals $(k = 1, 2, \ldots, n)$ in the matrix

form:

$$\begin{cases} \boldsymbol{P_x} = \boldsymbol{U}\boldsymbol{x}, \\ \boldsymbol{P_y} = \boldsymbol{U}\boldsymbol{y}, \\ \boldsymbol{P_x} = \left[p_{x1}, p_{x2}, \ldots, p_{x(n-1)}, p_{xn}\right]^{\mathrm{T}}, \\ \boldsymbol{P_y} = \left[p_{y1}, p_{y2}, \ldots, p_{y(n-1)}, p_{yn}\right]^{\mathrm{T}}, \\ \boldsymbol{x} = \left[x_1, x_2, \ldots, x_{n-1}, x_n\right]^{\mathrm{T}}, \\ \boldsymbol{y} = \left[y_1, y_2, \ldots, y_{n-1}, y_n\right]^{\mathrm{T}}, \\ \boldsymbol{U} = \begin{pmatrix} u_1+v_1, w_1, 0 & \cdots & \boldsymbol{0} \\ u_2,\ v_2,\ w_2 & & \\ \vdots & & \vdots \\ \boldsymbol{0} & \cdots & u_{n-1}, v_{n-1}, w_{n-1} \\ & & 0,\ u_n,\ v_n+w_n \end{pmatrix}. \end{cases} \tag{11}$$

The discretized COM trajectory can be calculated as follows:

$$\boldsymbol{x} = \boldsymbol{U}^{-1}\boldsymbol{P_x}, \quad \boldsymbol{y} = \boldsymbol{U}^{-1}\boldsymbol{P_y}. \tag{12}$$

With the algorithm based on the cart-table model, we are sure that COM locations will be adjusted to make sure that the outputs of ZMP locations are consistent with the planned ones. Thus, the stable robot movement that we desire can be realized. Nevertheless, both algorithms described above belong to off-line methods, which means that they have to calculate the entire trajectory off-line to generate a continuous walking pattern.

4.2.3 Bipedal walking pattern generation based on ZMP preview control

To realize online walking pattern generation, an algorithm based on ZMP preview control is introduced in this subsection. First, a new vector $\boldsymbol{s} = (s_x, s_y)$ is defined as follows:

$$s_x = \frac{\mathrm{d}}{\mathrm{d}t}\ddot{x}, \quad s_y = \frac{\mathrm{d}}{\mathrm{d}t}\ddot{y}. \tag{13}$$

Regarding $\boldsymbol{s}$ as the input of Eq. (9), the ZMP location equation about x can be translated into a servo control system as follows:

$$\begin{cases} \dfrac{\mathrm{d}}{\mathrm{d}t}\begin{bmatrix} x \\ \dot{x} \\ \ddot{x} \end{bmatrix} = \begin{bmatrix} 0 & 1 & 0 \\ 0 & 0 & 1 \\ 0 & 0 & 0 \end{bmatrix}\begin{bmatrix} x \\ \dot{x} \\ \ddot{x} \end{bmatrix} + \begin{bmatrix} 0 \\ 0 \\ 1 \end{bmatrix} s_x, \\ P_x = \begin{bmatrix} 1 & 0 & -\dfrac{z_{\mathrm{c}}}{g} \end{bmatrix}\begin{bmatrix} x \\ \dot{x} \\ \ddot{x} \end{bmatrix}. \end{cases} \tag{14}$$

For the equation about y, we can deal with the same form; thus, it will be omitted in the following parts. System (14) can be discretized with sampling time (Δt):

$$\begin{cases} \boldsymbol{r}_{k+1} = \boldsymbol{A}\boldsymbol{r}_k + \boldsymbol{B}s_{xk}, \\ P_{xk} = \boldsymbol{C}\boldsymbol{r}_k, \\ \boldsymbol{r}_k \equiv \left[x\left(k\Delta t\right),\ \dot{x}\left(k\Delta t\right),\ \ddot{x}\left(k\Delta t\right)\right]^{\mathrm{T}}, \\ \boldsymbol{A} \equiv \begin{bmatrix} 1 & \Delta t & \Delta t^2/2 \\ 0 & 1 & \Delta t \\ 0 & 0 & 1 \end{bmatrix}, \\ \boldsymbol{B} \equiv \begin{bmatrix} \Delta t^3/6 \\ \Delta t^2/2 \\ \Delta t \end{bmatrix}, \\ \boldsymbol{C} \equiv \left[\,1 \quad 0 \quad -z_{\mathrm{c}}/g\,\right]. \end{cases} \tag{15}$$

With the reference ZMP location P_{xk}^{ref}, the performance index J can be defined as

$$J = \sum_{i=k}^{\infty}\left(Q_e e_i^2 + \Delta\boldsymbol{r}_i^{\mathrm{T}}\boldsymbol{Q_r}\Delta\boldsymbol{r}_i + Q_s\Delta s_{xi}^2\right), \tag{16}$$

where $e_k \equiv P_{xk}^{\mathrm{ref}} - P_{xk}$, $\Delta\boldsymbol{r}_k \equiv \boldsymbol{r}_k - \boldsymbol{r}_{k-1}$, and $\Delta s_{xk} \equiv s_{xk} - s_{xk-1}$. Q_e, Q_s, and $\boldsymbol{Q_r}$ are weighting factors.

With N_{L} step future reference ZMP locations at every sampling time, the input s_{xk} in Eq. (15) can be obtained as Eq. (17) by minimizing index J, and s_{yk} can be calculated in the same way:

$$s_{xk} = -K_e\sum_{i=0}^{k} e_i - \boldsymbol{K_r}\boldsymbol{r}_k + \sum_{j=1}^{N_{\mathrm{L}}} K_{Pj}P_{xk+j}^{\mathrm{ref}}, \tag{17}$$

where K_e, $\boldsymbol{K_r}$, and K_{Pj} are the gains ($\boldsymbol{K_r} \in \mathbb{R}^{1\times 3}$).

As Fig. 9 shows, the ZMP preview control system consists of three parts: a first-in-first-out (FIFO) buffer for storing N_{L} step future reference ZMP locations, a preview controller for calculating the input of the control system, and a cart-table dynamic model for calculating the state of the system. With this algorithm, we can generate a continuous walking pattern online.

5 Numerical research and preliminary experiments

In this section, numerical research on the three algorithms is implemented for comparison. The algorithm based on ZMP preview control is finally chosen

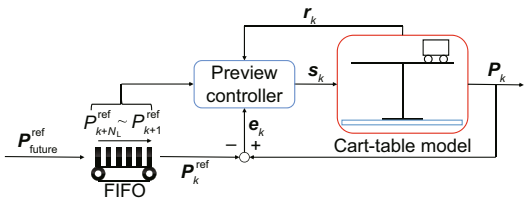

Fig. 9 Architecture of ZMP preview control

to generate the walking pattern for the walking experiment on a flat terrain, which aims at validating the self-balanced walking ability of Auto-LEE.

The Auto-LEE virtual prototype is built according to the design presented in Section 3, and the total mass of the robot is 42 kg. As Fig. 10a shows, the initial state of the exoskeleton is set as follows: (1) the COM is constrained in a horizontal plane $z_c = 0.85$ m; (2) the initial position of the COM is $\boldsymbol{P}_O = [0, -0.125, 0.85]$ m; (3) the initial location of the left/right foot is $\boldsymbol{P}_L = [0, 0.125, 0.133]$ m / $\boldsymbol{P}_R = [0, 0.125, -0.133]$ m; (4) the lift height of the swing foot is $h_z = 0.1$ m; (5) the initial velocity and acceleration of the whole body are set at zero.

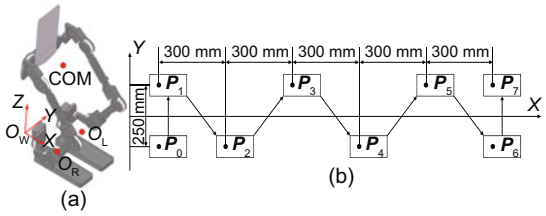

Fig. 10 Virtual prototype (a) and planned foot locations (b)

The planned foot locations are set as Fig. 10b shows: the exoskeleton walking along the x axis with seven steps on a flat terrain. The step parameters are set as in Table 4, and the gait cycle is $T_s = 1$ s. For the algorithm based on 3D-ILPM, the conditions are set as $a_x = b_x = a_y = b_y = 1$. For the algorithm based on the cart-table model, the sampling time is set as $\Delta t = 5$ ms. The conditions of the algorithm based on ZMP preview control are set as $N_L = 400$, $Q_e = 1$, $Q_s = 1 \times 10^{-7}$, $\boldsymbol{Q_r} = \boldsymbol{0}$.

Table 4 Planned foot locations

Step (n)	1	2	3	4	5	6	7
S_x^n (mm)	0	300	300	300	300	300	0
S_y^n (mm)	250	250	250	250	250	250	250

With these initial conditions and the exoskeleton parameters, the walking patterns are generated using the three different algorithms (Fig. 11). As the figure shows, the foot trajectory generated with the 3D-ILPM model is off the planned one; actually this result cannot be applied to practical use. On the contrary, the trajectories generated with the cart-table model and ZMP preview control are almost consistent with the desired one.

To generate the walking patterns that we desire in a continuous way, we adopt the online algorithm based on ZMP preview control. For the experiment, the gait cycle is set as $T_s = 3$ s, and the sampling time is $\Delta t = 5$ ms. The future reference factor N_L is determined as $N_L = 2\,T_s/\Delta t = 1200$, $Q_e = 1$, $Q_s = 1 \times 10^{-7}$, and $\boldsymbol{Q_r} = \boldsymbol{0}$. The preview action gain K_{Pj} is shown in Fig. 12, which indicates that the gain is almost zero when $N_L \geq 1200$.

The calculated ZMP trajectory (blue thin spline) and COM trajectory (green circle spline)

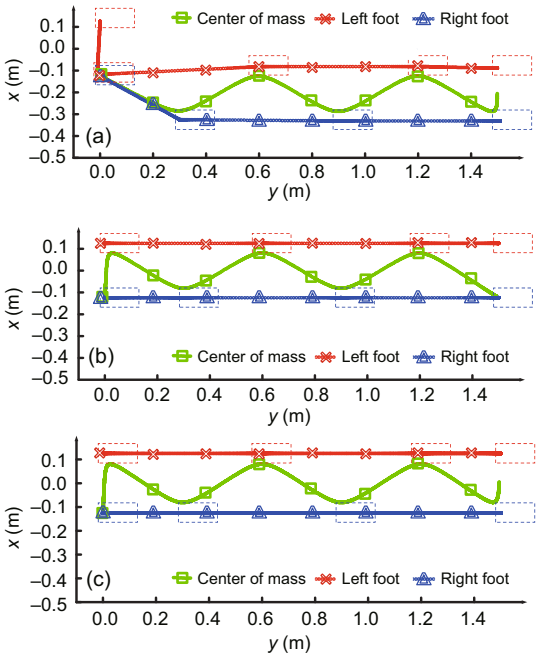

Fig. 11 Numerical results: generated trajectories with 3D-ILPM (a), cart-table model (b), and ZMP preview control (c)

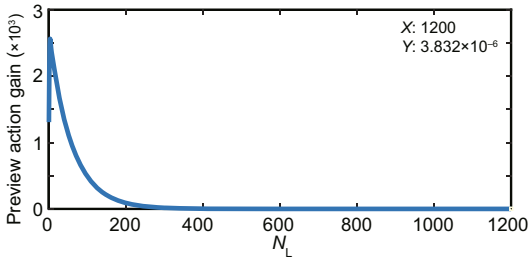

Fig. 12 Preview action gains

are shown in Fig. 13, and the red dotted spline is the planned ZMP trajectory. The maximum ZMP tracking error in the x direction is $\Delta\text{ZMP}_x = 0.0805$ m, and the one in the y direction is $\Delta\text{ZMP}_y = 0.0671$ m. From the numerical analysis, we find that the tracking error is inversely proportional to factor Q_e. When $Q_e = 1000$, the tracking errors become $\Delta\text{ZMP}_x = 4.76 \times 10^{-4}$ m and $\Delta\text{ZMP}_y = 1.1 \times 10^{-3}$ m.

With the algorithm based on ZMP preview control, the COM trajectory and both foot trajectories are obtained under the initial conditions described above. We can input these trajectories into the Auto-LEE inverse kinematic model. Then the angles of the 10 joints (q1–q10) of the exoskeleton are calculated (Fig. 14). In the last process, we consider the offset between the COM and the center of the waist, but the difference caused by the simplified cart-table model and the precise multi-body dynamics is ignored, which may amplify the ZMP tracking error.

The real Auto-LEE prototype has been developed, and we drove the exoskeleton in an open-loop form with the joint angles calculated above. As Fig. 15 shows, preliminary self-balanced walking is realized.

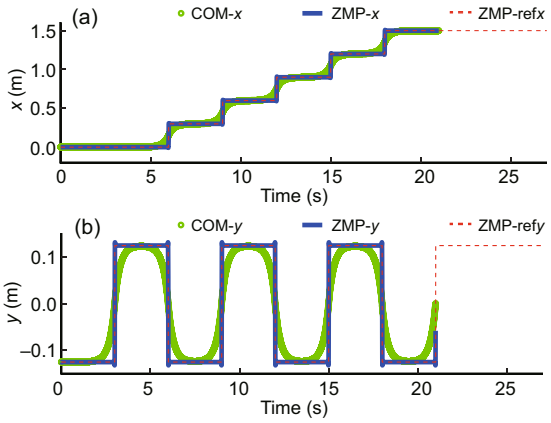

Fig. 13 Numerical results: generated trajectories in the x direction (a) and y direction (b). References to color refer to the online version of this figure

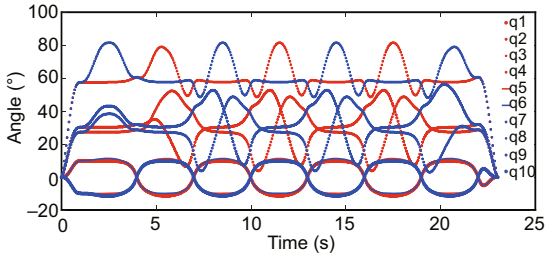

Fig. 14 Calculated angles of the joints

Fig. 15 Snapshots of a self-balanced walking experiment on a flat terrain

To further validate the self-balancing ability of Auto-LEE, a walking experiment with the robot carrying a dummy on a flat terrain was implemented. The height of the dummy is 1.62 m, and its weight is 20 kg. Using the gait planned with the previously described planning method, Auto-LEE realized stable walking on the flat concrete ground (Fig. 16), even though the swing of the unconstrained arms of the dummy introduced a small disturbance during walking. Because the robot is controlled in an open-loop form, currently it is unable to walk stably on a rough terrain, and a large external disturbance will cause the robot to fall down. The dynamic balanced walking at a faster speed within a complex walking environment will be studied in our future work.

Fig. 16 Snapshots of self-balanced walking experiment with a dummy on a flat terrain

6 Conclusions and future work

For the lack of active DOFs, patients wearing traditional exoskeletons may suffer from problems like interference and unnatural gait while walking. In addition, users have to spend a lot of time and energy in practicing to maintain their balance with crutches. To solve this dilemma, we have proposed a novel autonomous lower extremity exoskeleton. The main results of this paper are as follows:

1. Biomechanical analysis on the human body has been performed, which indicates that the abduction/adduction motions of the joints in the coronal plane play an important role in maintaining balance in bipedal walking.

2. With modular structure design and multi-modal human-robot interfaces, the exoskeleton can

be applied to users of different sizes and with different conditions. For example, a paraplegic can handle a device with a joystick, and a tetraplegic can control a device with EEG equipment.

3. Three general algorithms for bipedal walking have been researched, and the preliminary experiment on a flat terrain has validated the self-balanced walking ability of Auto-LEE. However, deviation from the original occurred during the experiment, which could be caused by the absence of a stabilizer controller and the simplification of the dynamical model.

In future work, we will focus on an autonomous trajectory planning method based on computer vision, a robust control algorithm to stabilize bipedal walking on a rough terrain in the case of human disturbance, and safety problems of human-robot interactions.

References

Brown-Triolo DL, Roach MJ, Nelson K, et al., 2002. Consumer perspectives on mobility: implications for neuroprosthesis design. *J Rehabil Res Dev*, 39(6):659-669.

Cenciarini M, Dollar AM, 2011. Biomechanical considerations in the design of lower limb exoskeletons. IEEE Int Conf on Rehabilitation Robotics, p.1-6. https://doi.org/10.1109/ICORR.2011.5975366

Fang Y, Yu Y, Chen F, et al., 2008. Dynamic analysis and control strategy of the wearable power assist leg. IEEE Int Conf on Automation and Logistics, p.1060-1065. https://doi.org/10.1109/ICAL.2008.4636308

Gao S, 2004. Practical Anatomical Atlas: Lower Limbs Volume. Shanghai Science and Technology Press, Shanghai (in Chinese).

Gardner AD, Potgieter J, Noble FK, 2017. A review of commercially available exoskeletons' capabilities. 24$^{\text{th}}$ Int Conf on Mechatronics and Machine Vision in Practice, p.1-5. https://doi.org/10.1109/M2VIP.2017.8211470

Kajita S, Kanehiro F, Kaneko K, et al., 2001. The 3D linear inverted pendulum mode: a simple modeling for a biped walking pattern generation. IEEE/RSJ Int Conf on Intelligent Robots and Systems, p.239-246. https://doi.org/10.1109/IROS.2001.973365

Kajita S, Kanehiro F, Kaneko K, et al., 2003. Biped walking pattern generation by using preview control of zero-moment point. IEEE Int Conf on Robotics and Automation, p.1620-1626. https://doi.org/10.1109/ROBOT.2003.1241826

Katayama T, Ohki T, Inoue T, et al., 1985. Design of an optimal controller for a discrete-time system subject to previewable demand. *Int J Contr*, 41(3):677-699. https://doi.org/10.1080/0020718508961156

Kong K, Jeon D, 2006. Design and control of an exoskeleton for the elderly and patients. *IEEE/ASME Trans Mech*, 11(4):428-432. https://doi.org/10.1109/TMECH.2006.878550

Kong K, Moon H, Hwang B, et al., 2009. Impedance compensation of SUBAR for back-drivable force-mode actuation. *IEEE Trans Rob*, 25(3):512-521. https://doi.org/10.1109/TRO.2009.2019786

Kopp C, 2011. Exoskeletons for warriors of the future. *Defence Today*, 9(2):38-40.

McDonald JW, Sadowsky C, 2002. Spinal-cord injury. *Lancet*, 359(9304):417-425. https://doi.org/10.1016/S0140-6736(02)07603-1

Mertz L, 2012. The next generation of exoskeletons: lighter, cheaper devices are in the works. *IEEE Pulse*, 3(4):56-61. https://doi.org/10.1109/MPUL.2012.2196836

Mori Y, Taniguchi T, Inoue K, et al., 2011. Development of a standing style transfer system able with novel crutches for a person with disabled lower limbs. *J Syst Des Dyn*, 5(1):83-93. https://doi.org/10.1299/jsdd.5.83

National Spinal Cord Injury Statistical Center, 2016. Spinal Cord Injury Facts and Figures at a Glance. https://www.nscisc.uab.edu/Public/Facts%202016.pdf

Protection B, Labour M, 1988. Human Dimensions of Chinese Adults, GB 10000-1988. National Standards of People's Republic of China (in Chinese).

Shimmyo S, Sato T, Ohnishi K, 2013. Biped walking pattern generation by using preview control based on three-mass model. *IEEE Trans Ind Electron*, 60(11):5137-5147. https://doi.org/10.1109/TIE.2012.2221111

Strausser KA, Swift TA, Zoss AB, et al., 2010. Prototype medical exoskeleton for paraplegic mobility: first experimental results. ASME Dynamic Systems and Control Conf, p.453-458. https://doi.org/10.1115/DSCC2010-4261

Talaty M, Esquenazi A, Briceño JE, 2013. Differentiating ability in users of the rewalk$^{\text{TM}}$ powered exoskeleton: an analysis of walking kinematics. IEEE Int Conf on Rehabilitation Robotics, p.1-5. https://doi.org/10.1109/ICORR.2013.6650469

Tsukahara A, Hasegawa Y, Eguchi K, et al., 2015. Restoration of gait for spinal cord injury patients using HAL with intention estimator for preferable swing speed. *IEEE Trans Neur Syst Rehab Eng*, 23(2):308-318. https://doi.org/10.1109/TNSRE.2014.2364618

Vukobratović M, Borovac B, 2004. Zero-moment point—thirty five years of its life. *Int J Humanoid Rob*, 1(1):157-173. https://doi.org/10.1142/S0219843604000083

Zhang SM, Wang C, Wu XY, et al., 2016. Real time gait planning for a mobile medical exoskeleton with crutche. IEEE Int Conf on Robotics and Biomimetics, p.2301-2306. https://doi.org/10.1109/ROBIO.2015.7419117

Zoss AB, Kazerooni H, Chu A, 2006. Biomechanical design of the Berkeley lower extremity exoskeleton (BLEEX). *IEEE/ASME Trans Mech*, 11(2):128-138. https://doi.org/10.1109/TMECH.2006.871087